Non-Destructive Measurement of Optically Scattering Polymer Films Using Image Processing

Noah M. McAllister[1], Robert A. Green-Warren[1], Maxim Arkhipov[1], Jae-Hwang Lee[2], Assimina A. Pelegri[1], Jonathan P. Singer[1]

[1] Department of Mechanical and Aerospace Engineering, Rutgers, The State University of New Jersey, 98 Brett Rd., Piscataway, NJ 08854

[2] Department of Mechanical and Industrial Engineering, University of Massachusetts, 160 Governors Drive, Amherst, MA 01003-2210

Abstract

We establish a sample- and data-processing pipeline that allows for high-throughput measurement optical microscope measurement of porous films, provided that the film is sufficiently optically scattering. Here, self-limiting electrospray deposition (SLED) is used to manufacture scattering films of different morphologies. This technique compensates for the scattering of the films through background subtraction of the reflection image with the transmission image. This process is implemented through a combination ImageJ-MATLAB data pipeline; the Canny edge-detector is used as the image-processing algorithm to identify boundaries of the film. We verify this process against manually measured images; a comparative study between cross-sectional scanning electron microscopy (where scattering effects are diminished) and optical microscopy also verifies that our optical microscopy technique can be used to consistently, non-destructively measure film thickness regardless of film morphology. In addition, this technique can be used in combination with dense film measurements to measure film porosity.

Introduction

There has been recent engineering interest in porous polymeric films, especially those with multi-scale features. These porous polymer films are of particular interest in separation membranes for energy-storage devices[1-4] and as precursor templates for porous carbon films[5-7]. These films are often optically scattering because their microstructure is non-uniform, and often so on a length scale of similar or smaller length than the incident wavelength[8,9]. Moreover, there has been research on bio-inspired, porous, thin films with the express purpose of being highly scattering; these films have use-cases in optoelectronics where whiteness and high-reflectivity are useful[10-12]. However, this scattering presents a difficulty in the thickness measurement of these films, as solid-thin film measurement techniques (e.g., reflectometry) cannot handle the high scatter. Currently, the above references use scanning electron microscopy (SEM) to characterize the thickness of the films; however, this is a destructive process because the polymer film needs to be coated in a conductive material. This motivates the process described herein, which uses image processing of optical micrographs to measure the thickness of optically scattering film.

Image processing is frequently used in the material sciences for characterization and analysis. Image processing has been used for the characterization of carbonyl iron powder/polyaniline composites[13], of nano-filler dispersion in polymer films[14], and of the lamellar structure of semi-crystalline polymers[15]. Specialized tools have been built for this purpose; for example, Dream3D was built for the 3-D microstructure characterization of electron backscatter diffraction data[16]. Advancement has also been made possible by the plethora of open- and closed-source general-purpose image processing libraries and applications such as ImageJ/Fiji[17,18], OpenCV[19], skikit image[20] and the MATLAB Image Processing Toolbox[21]. In the described method, we make use of ImageJ and the MATLAB Image Processing Toolbox.

https://doi.org/10.26434/chemrxiv-2023-88szt ORCID: https://orcid.org/0000-0002-5934-8795

In this study, we utilize electrospray deposition (ESD), a manufacturing technique that uses a high potential difference to atomize a solution into constituent droplets through Coulombic fission which are then deposited on a substrate to produce optically scattering samples. The particular regime of ESD that we use is self-limiting electrospray deposition (SLED). SLED is a regime of ESD that utilizes charge repulsion for coating complex 3D surfaces and 2D templated patterns with polymer composites[22-27]. SLED has three benefits that make it an ideal method for creating optically scattering polymer films: 1) deposition via SLED is conformal, meaning that it can coat complex geometries without needing to move the spray needle[24], 2) the deposition process is relatively quick and does not require any type of immersion, leading to a high-throughput manufacturing process; and 3) the deposition consists of a hierarchical structure of hollow polymer shells or wires, which provides several functional advantages, but leads to a highly scattering film comprised of otherwise low refractive index materials similar to any other open cell foam[28].

The scattering nature of SLED films means that it cannot be measured by optical film measurement techniques, such as reflectometry. Therefore, previous studies of SLED films have used an equivalent densified thickness in-place of the true porous thickness of the film[22,26,27]. This was done by heating the polymer above the glass-transition temperature T_g to collapse the porous morphology; measurement was conducted using an optical reflectometer[22,24,26,27]. This behavior is shown in Figure 1a-b, which shows a schematic of the densification process. A polystyrene (PS) SLED sample manufactured in the same conditions is shown in Figure 1c in the porous (as-manufactured) and densified states (post-heating).

Here, a method of non-destructively measuring scattering polymer films is described; it uses a validated[29] MATLAB-based image-processing algorithm to measure film thickness in optical micrographs. We demonstrate the applicability of this technique by measuring the thickness of films of different compositions: PS, methylcellulose (MC), and SU-8 epoxide photoresist. From previous work, we have shown that these polymers exhibit different micro-morphologies, while the optical scattering remains relatively consistent[22,24-27].

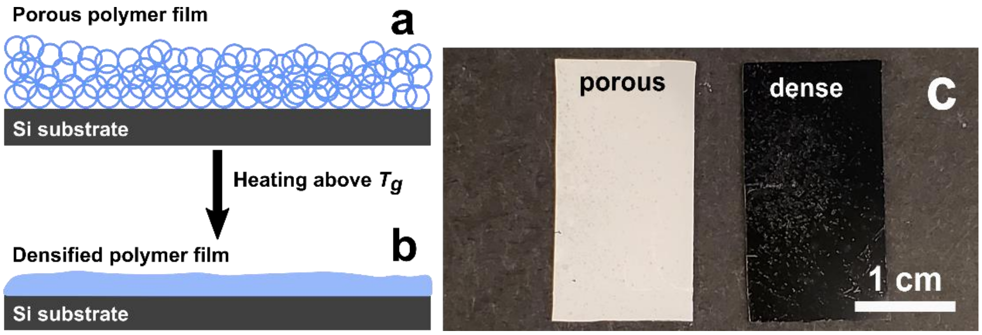

Figure 1. (a) A cross-sectional schematic of the hollow sphere (porous) morphology of the film. (b) Cross-sectional schematic of the film after thermal densification. (c) A top-down camera image of ~20 µm thick PS 35 kDa SLED film in both the porous (left) and dense (right) states.

Methods

Precursor solutions

PS (35 kDa and 280 kDa, Sigma-Aldrich), SU-8 (EPON Resin SU-8), and MC (15 kDa, Sigma-Aldrich)were used as received. 2-butanone (>99% Sigma-Aldrich) and anhydrous 200 proof pure ethanol (Sigma-Aldrich) were used as received as the carrier solvents for electrospray solution. PS and SU8 were sprayed in pure 2-butanone, and MC was sprayed in a 3:2 wt. solution of the deionized water and anhydrous ethanol. Solutions were mixed to 1% wt.

Self-limiting electrospray deposition procedure

The ESD procedure, in general, follows the procedure by Green-Warren et al.[22] The ESD setup consists of a syringe pump (KD Scientific KDS-100), two high-voltage potential supplies (Matsusada Precision Inc., RB30-30P), the stainless-steel delivery needle (SAI Infusion, 20 gauge, 1.5″), and the steel extractor ring (inner diameter of 2 cm and an outer diameter of 4 cm). The solution was delivered by a disposable syringe (5 mL NORM-JECT), connected to the spray delivery needle using 1/32″ polytetrafluoroethylene tubing (Cole-Parmer Instrument Company). High-voltage potential supplies were connected (1) delivery needle and (2) extractor ring. Spray was collected on ~2.5 cm × ~2 cm rectangular silicon chips, which rested on 10 cm diameter silicon wafers (both University Wafer, Boron-doped P-type 0-100 Ohm-cm). The base wafer was electrically grounded during the spray. The silicon chips were diamond scribed along on the back of the chip to facilitate post-spray fracturing. The scribing line was parallel to the long edge of the chip and located close to the center of the chip's shorter dimension. All silicon wafers and chips were cleaned and degreased with ethanol and acetone prior to spray.

Electrospray conditions

Taylor-cone jet sprays were used for all samples. The driving voltage on the delivery needle was set to 6.0 kV. The extractor ring voltage was varied between 2.6 and 4.5 kV in order to maintain stability of the Taylor-cone. The needle tip-to-sample spray distance was set to 4 cm, and the extractor ring was located 1 cm above the needle tip. A flow rate of 0.5 mL/h was used for all PS and SU8 samples; the flowrate of MC samples was varied between 0.06 and 0.18 mL/h[25]. The substrate temperature was controlled using a hotplate. The humidity was monitored and ranged between 13% and 66% relative humidity. A full description of spray parameters can be found in Table S1.

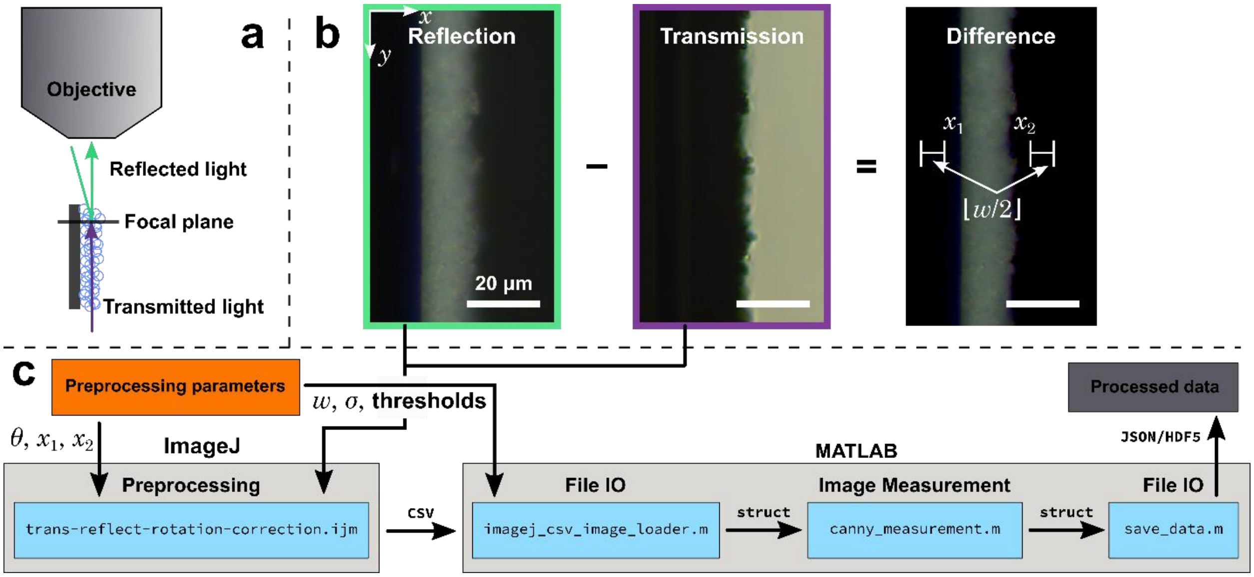

Figure 2. (a) Cross-sectional schematic of optical microscopy system, showing sample imaged with reflected (green) and transmitted (purple) light. (b) Corresponding images of the same porous PS 35 kDa sample, taken in reflection and transmission mode. In some cases, it is useful to use the difference of the reflection and transmission images. (c) The structure of the image measurement software is shown.

Image acquisition

Samples used for optical microscopy were prepared by fracturing spray samples near the center of spray at room temperature with diamond scribe-prescribing to expose of a cross-section of material. Samples were then mounted vertically on a square steel reference block using vacuum grease (Dow Corning High Vacuum Grease) as a surface adhesive, such that the spray is on the outside of the block, and the cross-sectional surface faces upward. The samples are then imaged in three measured locations along its length. Images were taken in both reflection and transmission modes using a Leica DM2700 M optical microscope with a Leica MC170 HD camera; the focal plane of the image remains constant in both modes. This procedure is shown in Figure 2a-b.

Image processing algorithm

The thickness of the film is calculated using the following procedure, using ImageJ and MATLAB. The measurement technique we present relies on four user-defined properties, excluding the input parameters of the edge detection algorithm used: the angle of the film from vertical θ, cropping locations x_1 and x_2, and a search width w; these parameters are shown in the orange box of Figure 2c. The angle θ, x_1, and x_2 are defined using an ImageJ macro, while w and the parameters to the edge detection algorithm (in this case, the standard deviation of the Gaussian σ and hysteresis thresholds). In order to ensure that the film edges are vertical and to determine a crop region, the user draws a line along spray-substrate interface in the reflection image in ImageJ. The angle θ of the film is determined using the slope of the user-drawn line; both the reflection and transmission images are transformed by θ such that the film is vertical. This user-drawn line is also used as the value for x_1. x_2 is determined in a similar manner: the user then selects an approximate location of the outer bounds of the spray from the transmission image. The transmission mode image is used as an approximation for the outer bounds of the film because the distinction between the film and the environment is more distinct than in the reflection mode image. This data is saved as a comma-separated value (CSV) file, which is then read into MATLAB for further measurement.

With the CSV created by the ImageJ macro, the images are loaded into data loader (`imagej_csv_image_loader.m`) in MATLAB, which passes the images by reference (via path) and the parameters by value to the measurement function (`canny_measurement.m`). The measurement function works as follows: the images are first cropped between $\left[x_1 - \left\lfloor\frac{w}{2}\right\rfloor, x_2 + \left\lfloor\frac{w}{2}\right\rfloor\right]$, and if the edge detection algorithm should be implemented on the difference of the reflection and transmission mode image, the difference is calculated (shown in Figure 2b). The image (reflection mode or difference image) is then converted to grayscale (necessary for edge detection). We make use of the Canny edge detection algorithm[29] to detect the interfaces of the spray. The Canny edge detector works by convolving a Gaussian kernel of standard deviation σ with the image to remove high frequency noise. The gradient operation is then applied, such as the Sobel or Roberts kernel. Edge thinning is then applied using non-maximal suppression. Double thresholding (shown as the "thresholds" in Figure 2c) then divides the edges into "strong" and "weak" edges, using two threshold values. "Strong" edges are pixels where the magnitude of the gradient is greater than the upper threshold, and weak edges are pixels where the magnitude of the gradient is between the threshold values. Edges in which pixels have gradient magnitudes less than the lower threshold are removed. Hysteresis is then used to remove any weak edges that are not also connected to strong edges. The following parameters were used in the aforementioned image processing algorithm in this study: we use low and high thresholds of 0.01 and 0.2 respectively and a Gaussian standard deviation of 10 pixels in the Canny edge detection function. A width w was chosen as 40 pixels. The transmission image was subtracted from the reflection image for the edge detection algorithm; its merit is discussed in the following section.

This approach of using the Canny algorithm is similar to the one used in Jordan et al[30]. To measure the thickness of the film, the difference of the location of detected outer points is calculated row-wise in the image. Rows with zero or only a single edge are discarded from the measurement. This array of measurement is then transformed from pixels to physical units of length via a conversion factor identified by ImageJ. One-variable statistical calculations are then performed on the thickness array. Processed data is output as a MATLAB `struct` object, and can be saved as a human-readable JavaScript Object Notation (JSON) or binary (but smaller file size) Hierarchical Data Format version 5 (HDF5) file via Qianqian Fang's JSONLab or EasyH5 respectively[31,32]. The merits of using this two-software system are discussed in the Results and Discussion section.

SEM Characterization

For select samples, 90° cross-sectional imaging using Zeiss Sigma field-emission scanning electron microscopy (SEM) was employed to verify measurement via optical microscopy, as scatter in SEM is reduced. Samples were prepared by fracturing spray samples near the center of spray at room temperature with diamond scribe-prescribing. These samples were then mounted on 90° stubs. Samples were sputter coated in ~10 nm of gold to prevent charging. Images acquired from SEM were measured manually in ImageJ: a line is drawn parallel to the substrate of the spray, and measurements were taken at uniform intervals perpendicular to the substrate line.

Porosity Measurement

For select samples (or sub-sections of samples), porosity can be estimated by densifying the material, and then measuring thickness using a microscopic reflectometer (Filmetrics F40). PS and SU-8 were densified by placing the sample on a hotplate for approximately 10 s at 120 °C and 80 °C, respectively. MC was densified by placing the sample in a -20 °C freezer for 10 min. and allowing to thaw to room temperature. At each location the sample was imaged in the optical microscope, a dense thickness in a 5×5 grid with 300 μm spacing (controlled with a Zaber E13F33E motorized stage) was recorded. For a given dense and porous thicknesses t_{dense} and t_{porous}, the porosity ϕ was calculated by

$$\varphi = 1 - \frac{t_{dense}}{t_{porous}}.$$

This is a first-order approximation that assumes the volume of deposited material is linearly proportional to its thickness. Correspondingly, uncertainty in porosity was calculated using the error propagation method described by Figliola and Beasley.[33]

Results and Discussion

Validation of measurement technique accuracy

As a test group, we use PS 35 kDa samples manufactured under the same conditions to test accuracy of this method. The accuracy of this method is tested first by validating that the edge detection method produces measurements that are comparable to those using manually-measured images. This comparison is shown in Figure 3a, where the thickness measured via image processing (Figure 3c) is plotted against the thickness of the same image, hand-measured in equal 10 μm increments by the authors (Figure 3b). The red line in the plot represents the equality of the measurement techniques. The majority of these measurements fall under this equality line, meaning that the manual thickness is greater than the image processing-measured image. However, we hypothesize this difference is due to the lack of defined edges within the image (the so-called "fuzziness"). When measuring micrographs manually, it is hard to determine the boundaries of the spray deposition, leading to possible overestimations. The image processing technique therefore has the advantage of the consistent determination of boundary locations.

Additionally, the variance of the measurements are approximately the same. This is explained by the roughness of the film – SLED produces a film that is highly stochastic, consisting of a random-packing of shellular droplets. This roughness has been observed before in both Lei et al. and Green-Warren et al., especially in materials that have a low glass transition temperature and are, therefore, not very self-limiting[22,27]. Overall, this means that the roughness of the film is greater than the error of the measurement, and this roughness is captured in both manual and automatic measurements. In order to test this statistically, a two-sided F-test of the equality of variances with a significance level of $\alpha = 0.05$ was performed on the data shown in Figure 3a: for all but one point, there was no significant difference between the two sets of measurements. It should be noted that this comparison is not testing the accuracy of the automatic measurement against the "true" thickness of the film: this comparison is done to show that the image processing method can produce more reliable measurements that manual measurement. Of course, the image processing method is much less labor intensive than manual measurement, leading to a high-throughput measurement method.

Since the thickness of images is comparable between hand measured and the aforementioned automatic procedure, the effects of background subtraction were quantified, as shown in Figure 3e. The scattering characteristic of the deposited film is shown in Figure 3d, where the reflection image is shown without background substraction. This scatter is reduced by subtracting the transmission image from the reflection image (Figure 3c); as such, the thickness of the film is greater when this scatter is not removed, as shown Figure 3e.

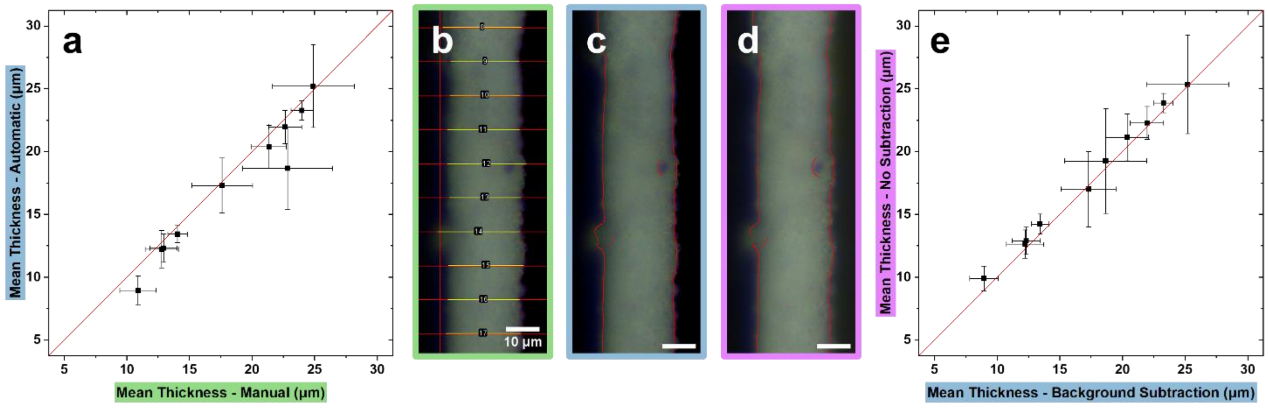

Figure 3. (a) Mean calculated thickness via image processing versus manual measurement for optical micrographs. (b-d) 225×600 pixel images of the same micrograph measured with different procedures: (b) was measured manually every 10 µm, shown in (green highlight), (c) was measured with image processing with transmission background subtraction (blue highlight), and (d) was measured with image processing without background subtraction (reflection image). (e) Mean thickness calculated via image processing: no transmission micrograph background subtraction versus transmission micrograph background subtraction. Error bars represent one standard deviation about the mean.

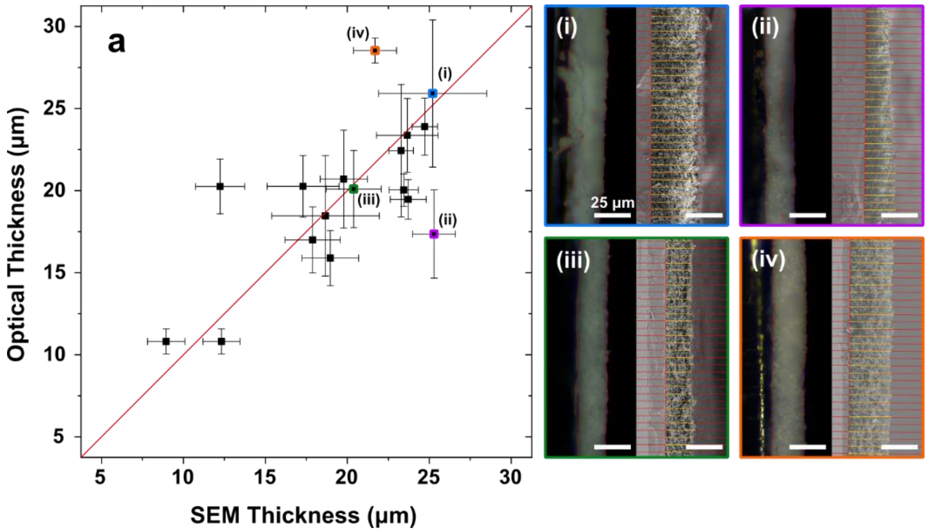

Figure 4. (a) Calculated thickness via image processing of optical micrographs versus manually measured thickness of SEM images. Red line represents equality of measurement techniques; above the line represents a larger optical measurement than SEM; below the line represents a larger SEM measurement than optical. (Colored boxes) Select images comparing optical (left) and SEM (right) measurements; (i, iii) represent good agreement between techniques, while (ii) has the larger optical measurements, and (iv) has larger SEM measurements. Error bars represent one standard deviation about the mean.

This measurement technique not only captures the roughness of the film, it also is validated by SEM measurements where scattering effects are less prevalent. This is shown in Figure 4a, a comparison of sample thickness is plotted against measured by manual SEM micrographs. Data above the equality line have a thicker measurement in optical measurement than SEM; data below has thicker SEM measurement than optical. Overall, this validates the optical technique in that there is close agreement between SEM and optical measurements. The callouts in the colored boxes show representative “good” agreement (i., iii.) for specific data. The primary error in these results in the possibility of the difference in location the measurements were taken from in the optical and SEM microscopes respectively. Even though the SLED process creates a relatively smooth deposition, there are still variations in thickness that are location-based[27]. From this figure, there is small trend towards SEM measurements being thicker than optical measurement; this could be due to a difference in locations. It is also possible that there is an inherent bias in the optical technique; however, this could be corrected for with calibration.

Extensibility and use-case of software

The primary benefit of this system of dual-program software is its extensibility, which serves to (1) create a system where the user can easily define sample-specific parameters, and (2) change between measurement systems without having to alter existing code structure. ImageJ comes with a built-in scripting (macro) language, and is interoperable with other programming languages, such as Python, JavaScript, and R.[18] We make use of the ImageJ scripting language as a means for the user to easily identify areas of the image that contain the relevant section of the image (i.e. the film). In addition, the technique is insensitive to user-inputted parameters, such as cropping width w and angle of rotation θ. The cropping width serves to reduce the effect of the user-bias of cropping region. The angle of rotation has minimal impact on the thickness because the angle of rotation is small (i.e., nearly vertical/horizontal images), so the thickness would be at most reduced by the cosine of the angle.

Because the output of the ImageJ script is a CSV file, this can be read into MATLAB, where the parameters of the image processing algorithm are also introduced. This parameter structure, which contains the locations of the image files, and all relevant image-processing parameters can be passed to an analysis algorithm(s). In this way, different segmentation and measurement algorithms could be "hot-swapped" for the Canny method used here as the use-case dictates.

Applicability of technique

An advantage of the measurement procedure described herein is its applicability to films of different morphologies. Because we use ESD to manufacture the scattering films, deposition morphology can be selectively controlled through tuning of spray parameters, such as solution composition and flowrate. We demonstrate this with shellular and nanowire porous films. For example, in Figure 5a (boxed), we validate the asymptotic thickness growth seen SLED of PS (sprayed at the same conditions) in the densified thickness initally measured by Lei et al.[27]. Additionally, the porous measurement allows for roughness that would be lost in densification to be captured in the measurement. Figure 5b shows similar asympotic thickness growth with time for PS sprayed at a lower temperature. SU-8 morphology is a fused network of agglomerated microspheres. SU-8 displays a more complex behavior than PS with a non-monotonic increase in thickness with increasing spray time (shown in Figure 5c.). While not the dicussion of this work, the authors hypothesize that the low glass-transition temperature of SU8 makes it susceptible to solvent densification in the manufacturing process. MC forms a morphology nanowire "forests" when sprayed using ESD; it is similarily optically scattering to PS[25,34]. Figure 5d. shows MC shows a flowrate series of MC where the mass deposited was kept constant. Through ESD, we create thin films of different morphologies; because they are optically scattering, the measurement system is able to measure the film regardless of the morphology.

This being mentioned, the film does not necessarily need to be manufactured through ESD. While we have demonstated its use case through ESD films, the criteria for this technique to work is that (1) the film is scattering under an optical microscope; (2) the films' thickness is resolvable by the optical microscope objective being used; and (3) a flat interface between the film and spray is clearly defined. Criterion (3) comes from fact the distance is measured as a distance between edge pixels. If an area-based segmentation approach were taken, a characteristic film thickness could be calculated for non-straight boundaries, assuming a boundary perimeter could be measured. As mentioned in criterion (1), the film must be scattering; as such, the measurement technique reaches its limit as the film becomes less scattering. In the case of ESD used here, as the spray temperature approaches the glass-transition temperature of the polymer, the porosity and morphological scattering is lowered as the material flows more easily[27]. However, this case of low scattering is not a concern because other optical measurement techniques (reflectometry, ellipsometry) could be used.

This measurement systems also allows for the porosity of the scattering sample (or a portion of the sample) to be calculated, assuming that there is a means of collapsing the morphology of the film. Because the materials used here are polymeric, samples can be condensed by heating the sample above the glass transition temperature, as shown in Figure 1. By assuming that the film thickness is directly proportional to the film volume, porosity could be calculated by measuring the change in height of the film before (with the system described herein) and after densification (e.g. with reflectometry). This was done for the samples shown in Figure 5b-d. Figure 5b. shows that the porosity of PS sprayed below its glass transition temperature remains relatively constant with increasing spray time. From a manufacturing point of view, this shows that there is not siginificant change in the way the particles of spray are being deposited after the asymptotic thickness limit is reached. The porosity of SU-8 is smaller than that of PS, due to its agglomerated nature. As previously mentioned, the butanone-SU-8 interaction is hypothesized to cause large variation in the porosity of the film. The MC displays the highest porosity, consistent with nanowire foam morphology and electron microscope imaging of the structure[25,34]. This technique avoids infiltration methods such as mercury porosimetry[35].

The primary benefit of this system is the fact that it is non-destructive, meaning that samples can be characterized and then used in other experiments, allowing the characterized region to be tested for (*e.g.*) mechanical, optical, catalytic, or biological functionality. There is no need to heat the film (to collapse the scattering morphology as necessiated by reflectometry) or coat the film in a conductive material (such as for SEM). A secondary advantage is that it is rapid, requiring only the acquisition of two optical images per mm of sample.

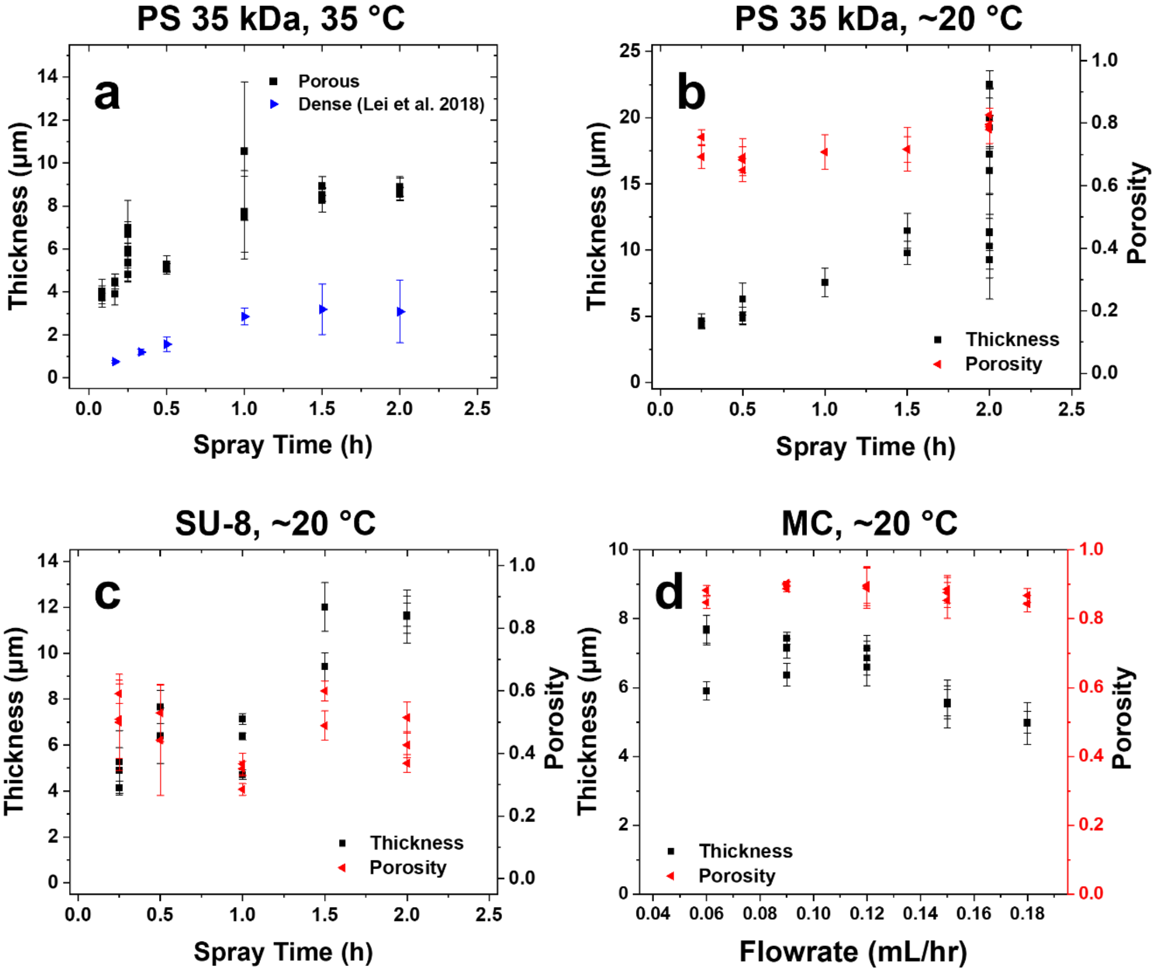

Figure 5. Thickness (left axis) plotted against ESD parameter (a—c spray time, d flowrate). (b—d) have an additional right axis (red)—porosity. Deposition material is PS (a,b), SU-8 (c), and MC (d).

Conclusion

Measurement of the thickness of porous (which often implies scattering) films are needed in a variety of applications; however, current techniques that can measure scattering films are destructive. We have shown a method of non-destructively measuring the thickness of these films using image processing of cross-sectional optical micrographs. We show this technique with an already-established edge-detection algorithm (by Canny); however, because of the easily extensible data framework, this algorithm could be easily changed. This technique is validated against both manually measured optical micrographs and SEM images. This technique is applicable to films of different compositions, thicknesses, and morphologies. In addition, the porosity can also be estimated if the porosity of the film can be collapsed and measured through a complementary optical technique, such as reflectometry or ellipsometry.

REFERENCES

1 Costa, C. M., Silva, M. M. & Lanceros-Méndez, S. Battery separators based on vinylidene fluoride (VDF) polymers and copolymers for lithium ion battery applications. *RSC Advances* **3**, 11404-11417 (2013). https://doi.org:10.1039/C3RA40732B

2 Horváth, D. V., Tian, R., Gabbett, C., Nicolosi, V. & Coleman, J. N. Quantifying the Effect of Separator Thickness on Rate Performance in Lithium-Ion Batteries. *Journal of The Electrochemical Society* **169**, 030503 (2022). https://doi.org:10.1149/1945-7111/ac5654

3 Jang, J., Oh, J., Jeong, H., Kang, W. & Jo, C. A Review of Functional Separators for Lithium Metal Battery Applications. *Materials* **13** (2020).

4 Lee, H., Yanilmaz, M., Toprakci, O., Fu, K. & Zhang, X. A review of recent developments in membrane separators for rechargeable lithium-ion batteries. *Energy & Environmental Science* **7**, 3857-3886 (2014). https://doi.org:10.1039/C4EE01432D

5 Liu, H. *et al.* Stepwise Crosslinking: A Facile Yet Versatile Conceptual Strategy to Nanomorphology-Persistent Porous Organic Polymers. *Advanced Materials* **29**, 1700723 (2017). https://doi.org:https://doi.org/10.1002/adma.201700723

6 Zeng, Q. *et al.* Template-free fabrication of hierarchical porous carbon based on intra-/inter-sphere crosslinking of monodisperse styrene–divinylbenzene copolymer nanospheres. *Chemical Communications* **46**, 5927-5929 (2010). https://doi.org:10.1039/C0CC00449A

7 Zou, C. *et al.* Template-free fabrication of hierarchical porous carbon by constructing carbonyl crosslinking bridges between polystyrene chains. *Journal of Materials Chemistry* **20**, 731-735 (2010). https://doi.org:10.1039/B917960G

8 Stover, J. C. *Optical Scattering: Measurement and Analysis*. 3 edn, (SPIE, 2012).

9 Schröder, S. *et al.* Origins of light scattering from thin film coatings. *Thin Solid Films* **592**, 248-255 (2015). https://doi.org:https://doi.org/10.1016/j.tsf.2015.02.077

10 Syurik, J., Jacucci, G., Onelli, O. D., Hölscher, H. & Vignolini, S. Bio-inspired Highly Scattering Networks via Polymer Phase Separation. *Advanced Functional Materials* **28**, 1706901 (2018). https://doi.org:10.1002/adfm.201706901

11 Syurik, J. *et al.* Bio-inspired, large scale, highly-scattering films for nanoparticle-alternative white surfaces. *Scientific Reports* **7**, 46637 (2017). https://doi.org:10.1038/srep46637

12 Tang, Y. *et al.* Bioinspired high-scattering polymer films fabricated by polymerization-induced phase separation. *Opt. Lett.* **45**, 2918-2921 (2020). https://doi.org:10.1364/OL.390639

13 Zhang, W., Zhang, F., Zhang, J., Zhang, J. & Zhang, J. Application of Digital Image Processing Technology in Polyaniline Deposition on the Surface of Carbonyl Iron Powder. *IOP Conference Series: Earth and Environmental Science* **252**, 022072 (2019). https://doi.org:10.1088/1755-1315/252/2/022072

14 Yildiz, K. & Yildiz, Z. Evaluation of nano-filler dispersion quality in polymeric films with binary feature characteristics and fractal analysis. *IET Image Processing* **14**, 2006-2012 (2020). https://doi.org:https://doi.org/10.1049/iet-ipr.2019.1512

15 Molnár, J. *et al.* Structural investigation of semicrystalline polymers. *Polymer Testing* **95**, 107098 (2021). https://doi.org:https://doi.org/10.1016/j.polymertesting.2021.107098

16 Groeber, M. A. & Jackson, M. A. DREAM.3D: A Digital Representation Environment for the Analysis of Microstructure in 3D. *Integrating Materials and Manufacturing Innovation* **3**, 56-72 (2014). https://doi.org:10.1186/2193-9772-3-5

17 Schindelin, J. *et al.* Fiji: an open-source platform for biological-image analysis. *Nature Methods* **9**, 676-682 (2012). https://doi.org:10.1038/nmeth.2019

18 Schneider, C. A., Rasband, W. S. & Eliceiri, K. W. NIH Image to ImageJ: 25 years of image analysis. *Nature Methods* **9**, 671-675 (2012). https://doi.org:10.1038/nmeth.2089

19 Bradski, G. The OpenCV Library. *Dr. Dobb's Journal of Software Tools* (2000).

20 van der Walt, S. *et al.* scikit-image: image processing in Python. *PeerJ* **2**, e453 (2014). https://doi.org:10.7717/peerj.453

21 *Image Processing Toolbox*, 2022).

22 Green-Warren, R. A. *et al.* Determining the Self-Limiting Electrospray Deposition Compositional Limits for Mechanically Tunable Polymer Composites. *ACS Applied Polymer Materials* **4**, 3511-3519 (2022). https://doi.org:10.1021/acsapm.2c00106

23 Grzenda, M. J. *et al.* Microscale Templating of Materials across Electrospray Deposition Regimes. *Coatings* **13**, 599 (2023).

24 Kovacevich, D. A. *et al.* Self-Limiting Electrospray Deposition for the Surface Modification of Additively Manufactured Parts. *ACS Applied Materials & Interfaces* **12**, 20901-20911 (2020). https://doi.org:10.1021/acsami.9b23544

25 Lei, L. *et al.* Homogeneous gelation leads to nanowire forests in the transition between electrospray and electrospinning. *Materials Horizons* **7**, 2643-2650 (2020). https://doi.org:10.1039/D0MH00872A

26 Lei, L. *et al.* Self-limiting electrospray deposition on polymer templates. *Scientific Reports* **10** (2020). https://doi.org:10.1038/s41598-020-74146-1

27 Lei, L. *et al.* Obtaining Thickness-Limited Electrospray Deposition for 3D Coating. *ACS Applied Materials & Interfaces* **10**, 11175-11188 (2018). https://doi.org:10.1021/acsami.7b19812

28 Höhler, R., Cohen-Addad, S. & Durian, D. J. Multiple light scattering as a probe of foams and emulsions. *Current Opinion in Colloid & Interface Science* **19**, 242-252 (2014). https://doi.org:https://doi.org/10.1016/j.cocis.2014.04.005

29 Canny, J. A Computational Approach to Edge Detection. *IEEE Transactions on Pattern Analysis and Machine Intelligence* **PAMI-8**, 679-698 (1986). https://doi.org:10.1109/tpami.1986.4767851

30 Jordan, J. L. *et al.* Elastic properties of polyethylene from high pressure sound speed measurements. *Polymer* **212**, 123164 (2021). https://doi.org:https://doi.org/10.1016/j.polymer.2020.123164

31 Fang, Q. *EasyH5 Toolbox*, 2022).

32 Fang, Q. *JSONLab*, 2022).

33 Figliola, R. S. & Beasley, D. E. *Theory and design for mechanical measurements*. 7 edn, (John Wiley & Sons, 2020).

34 Nachtigal, C. J. *et al.* Atomic Layer Deposition Reinforcement of Methylcellulose Nanowire Forests. *Advanced Engineering Materials* **24**, 2101485 (2022). https://doi.org:https://doi.org/10.1002/adem.202101485

35 Giesche, H. Mercury Porosimetry: A General (Practical) Overview. *Particle & Particle Systems Characterization* **23**, 9-19 (2006). https://doi.org:https://doi.org/10.1002/ppsc.200601009